Author/s:
Endrikat, S;Modesti, D;García-Mayoral, R;Hutchins, N;Chung, D

Title:
Kelvin–Helmholtz rollers in turbulent flow over riblets

Date:
2018-01-01

Citation:
Endrikat, S., Modesti, D., García-Mayoral, R., Hutchins, N. & Chung, D. (2018). Kelvin–Helmholtz rollers in turbulent flow over riblets. Proceedings of the 21st Australasian Fluid Mechanics Conference, AFMC 2018, Australasian Fluid Mechanics Society.

Persistent Link:
https://hdl.handle.net/11343/252857

21st Australasian Fluid Mechanics Conference
Adelaide, Australia
10-13 December 2018

# Kelvin–Helmholtz Rollers in Turbulent Flow over Riblets

**S. Endrikat[1], D. Modesti[1], R. García-Mayoral[2], N. Hutchins[1] and D. Chung[1]**

[1]Department of Mechanical Engineering, The University of Melbourne, Victoria 3010, Australia

[2]Department of Engineering, University of Cambridge, Cambridge CB2 1PZ, UK

## Abstract

Structures resulting from a Kelvin–Helmholtz instability have been shown to contribute to skin-friction drag in turbulent flow over blade-shaped riblets [4]. Using Direct Numerical Simulation (DNS) data, the present survey of several different riblet shapes reveals that the contribution to wall-shear stress due to the Kelvin–Helmholtz instability depends on riblet shape, in addition to a previously known dependence on riblet size. For a given drag change, sharp triangular and blade riblets promote development of the instability whilst blunt triangular and trapezoidal riblets appear to suppress it.

## Introduction

Riblets are streamwise-aligned surface grooves with sizes on the order of 10 viscous units, that have the potential to reduce skin-friction drag compared to a smooth wall. They are classified as passive flow control devices as no energy input is required to favourably alter the flow field, making them attractive for aerodynamic, maritime and petroleum engineering. Laboratory tests have shown that riblet shapes suitable for engineering applications can reduce drag by up to 8.2 % at $Re_\tau \lesssim 700$ [1].

The mechanism by which riblets reduce drag has been the subject of many studies [1, 9]. Streamwise vortices near the wall induce lateral flow fluctuations. Small riblets dampen these fluctuations, displacing the vortices upward and locally reducing the skin friction as near-wall turbulence is weakened [9, 4]. Using the skin friction coefficient $C_f = 2/U_{CL}^{+2}$, drag reduction compared to a smooth wall is defined as $DR = 1 - C_f/C_{f,\text{smooth}}$. In the viscous regime of small groove sizes, $DR$ increases linearly with viscous-scaled riblet spacing $s^+ = su_\tau/\nu$ with a slope determined by viscous theory [9]. The superscript + denotes viscous scaling using the kinematic viscosity $\nu$ and friction velocity $u_\tau \equiv \sqrt{\tau_w/\rho}$, which, in turn, is defined by the density $\rho$ and wall shear stress $\tau_w$. For $s^+ \gtrsim 15$, riblet tips of conventional geometries interfere directly with turbulent structures [8] and riblets with $s^+ \gtrsim 25$ increase drag compared to a smooth wall [1]. For small changes in drag, $DR \propto \Delta U^+$, where $\Delta U^+ = U^+_{\text{smooth}} - U^+$ is a shift in the profile of mean streamwise velocity compared to that of a smooth wall at matched height in or above the logarithmic layer. At $Re_\tau = 395$, $DR \approx -0.1\Delta U^+$. The breakdown of the drag-reducing regime was shown to scale with the square-root of the groove cross-sectional area, $\ell_g^+$. This scaling captures the drag change of various riblet shapes near their optimum sizes at $\ell^+_{g,\text{opt}} \approx 10.7$ [4]. Multiple mechanisms have been proposed to be responsible for increasing drag of a grooved surface compared to the optimally scaled geometry. Streamwise vortices above the wall are assumed to increase skin friction inside the riblet valley by sweeping streamwise momentum into the grooves when the tip spacing exceeds their diameter [2]. Another explanation for drag increase is that lateral velocity fluctuations are not damped when riblets are widely spaced, which allows them to interact with the geometry to produce secondary flow that transports streamwise momentum into the grooves [6]. More recently, García-Mayoral and Jiménez [4] discovered that an inflection point in the profile of mean streamwise velocity and a vertical permeability at the crest that increases with riblet size, give rise to a Kelvin–Helmholtz instability, which contributes to Reynolds shear stress and enhances drag. In this survey of six different riblet shapes, we further investigate the occurrence of the Kelvin–Helmholtz instability and measure its contribution to skin-friction drag as a function of riblet shape, size and drag change $\Delta U^+$.

## Numerical Setup

We conduct DNS to solve the Navier–Stokes equations of fluid motion in channels using Cascade's Cliff, which is a second-order accurate node-based collocated finite volume incompressible flow solver for unstructured grids. Domains are periodic in wall-parallel directions and a constant pressure gradient drives the channel flow at $Re_\tau = 395$. Riblets form the no-slip bottom surface and are resolved by the computational mesh, while a slip wall is located at the half-channel height $\delta$ above the riblet mean-height. All simulations of flow over riblets for this study employ the minimal-span channel concept [10], which reduces the computational cost while providing accurate estimates of drag for a given surface. In channels with small spanwise extent $L_y^+$, the velocity profile diverges from that of a full-span channel for heights $z^+ > z_c^+$, where $z_c^+ \approx 0.4L_y^+$ provided that this location is in the logarithmic layer [10]. For the present study, the condition was met by choosing $L_y^+ \gtrsim 250$ such that $z_c^+ \gtrsim 100$. Drag change with respect to a smooth wall full-span channel, $\Delta U^+$ is evaluated at $z^+ = z_c^+$ to obtain a result that does not depend on the channel width.

## Results

The six riblet shapes considered in this study are trapezoidal with opening angle $\alpha = 30°$, triangular with $\alpha = 30°, 60°$ and $90°$, asymmetric triangular with fixed $\alpha = 63.4°$ and blade riblets with a spacing-to-thickness ratio $s/t = 5$. Geometrical para-

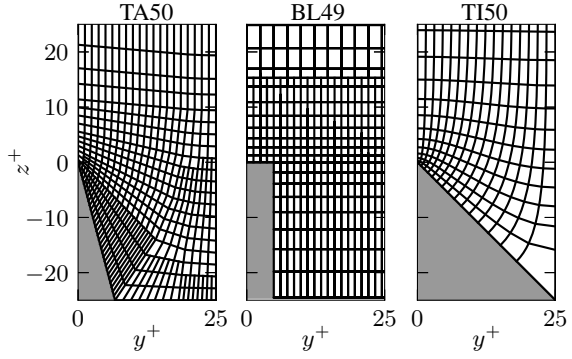


Figure 1: Meshes for different riblet geometries showing every fourth wall normal node. The solver supports meshes with hanging nodes. View spans half a riblet period of the symmetric mesh between the crest and centre of the groove.

| | Case | $s^+$ | $k^+$ | $\ell_g^+$ | $\alpha$ | $\Delta x^+$ | $\Delta y^+_{min} - \Delta y^+_{max}$ | $\Delta z^+_{min} - \Delta z^+_{max}$ | $L_x^+$ | $L_y^+$ | $\Delta T u_\tau/\delta$ |
|---|---|---|---|---|---|---|---|---|---|---|---|
| Trapezoidal | TA18 | 17.9 | 8.9 | 11.8 | 30.0° | 6.0 | 1.5 – 5.0 | 0.90 – 6.0 | 2054 | 250 | 50.8 |
| | TA31 | 31.3 | 15.6 | 20.6 | 30.0° | 6.0 | 1.5 – 5.0 | 0.90 – 6.0 | 2054 | 250 | 55.9 |
| | TA36 | 36.5 | 18.2 | 24.0 | 30.0° | 6.0 | 1.5 – 5.0 | 0.90 – 6.0 | 2054 | 255 | 42.8 |
| | TA50 | 50.0 | 25.0 | 32.9 | 30.0° | 6.0 | 1.5 – 5.0 | 0.90 – 6.0 | 2054 | 250 | 65.6 |
| | TA63 | 62.5 | 31.3 | 41.1 | 30.0° | 6.0 | 1.5 – 5.0 | 0.90 – 6.0 | 2054 | 250 | 47.1 |
| Symmetric triangular | TI10 | 10.1 | 18.8 | 9.75 | 30.0° | 6.0 | 0.057 – 1.5 | 0.033 – 7.0 | 1027 | 252 | 30.2 |
| | TI21 | 21.1 | 39.4 | 20.4 | 30.0° | 6.0 | 0.12 – 3.2 | 0.023 – 6.9 | 1027 | 253 | 38.5 |
| | TI15 | 14.7 | 12.7 | 9.68 | 60.0° | 6.0 | 0.083 – 2.2 | 0.041 – 7.0 | 1027 | 250 | 63.1 |
| | TI35 | 35.0 | 30.3 | 23.0 | 60.0° | 6.0 | 0.16 – 4.9 | 0.014 – 4.7 | 1027 | 245 | 59.7 |
| | TI19 | 19.2 | 9.6 | 9.60 | 90.0° | 6.0 | 0.11 – 2.9 | 0.047 – 7.1 | 1027 | 250 | 102 |
| | TI50 | 50.0 | 25.0 | 25.0 | 90.0° | 6.0 | 0.23 – 7.1 | 0.029 – 7.0 | 1027 | 250 | 95.5 |
| Asymmetric triangular | AT15 | 14.7 | 7.4 | 7.36 | 63.4° | 6.5 | 1.5 – 5.0 | 0.40 – 6.0 | 1027 | 250 | 27.6 |
| | AT20 | 19.2 | 9.6 | 9.62 | 63.4° | 6.5 | 1.5 – 5.0 | 0.40 – 6.0 | 1027 | 250 | 53.1 |
| | AT30 | 31.3 | 15.6 | 15.6 | 63.4° | 6.5 | 1.5 – 5.0 | 0.40 – 6.0 | 1027 | 250 | 13.6 |
| | AT40 | 41.7 | 20.8 | 20.8 | 63.4° | 6.5 | 1.5 – 5.0 | 0.40 – 6.0 | 1027 | 250 | 60.7 |
| | AT50 | 50.0 | 25.0 | 25.0 | 63.4° | 6.5 | 1.5 – 5.0 | 0.40 – 6.0 | 1027 | 250 | 36.5 |
| Blade | | | | | $s/t$ | | | | | | |
| | BL20 | 20.4 | 10.2 | 12.9 | 5.0 | 6.0 | 0.51 – 2.1 | 0.31 – 7.1 | 1031 | 265 | 100 |
| | BL34 | 33.5 | 16.8 | 21.2 | 5.0 | 6.0 | 0.85 – 3.4 | 0.31 – 7.1 | 1033 | 268 | 134 |
| | BL40 | 39.3 | 19.6 | 24.8 | 5.0 | 6.1 | 1.00 – 4.0 | 0.31 – 7.1 | 1035 | 275 | 141 |
| | BL49 | 49.0 | 24.5 | 31.0 | 5.0 | 6.0 | 1.2 – 4.9 | 0.30 – 6.7 | 1027 | 294 | 114 |

Table 1: Geometrical parameters, mesh spacings $\Delta^+$ and domain sizes $L^+$. The time interval $\Delta T$ is used to gather flow statistics.

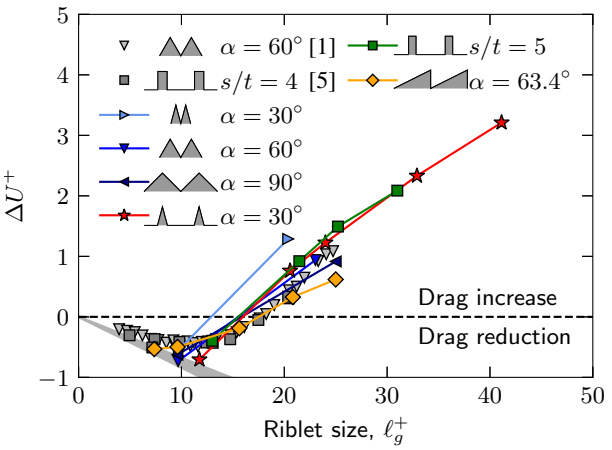


Figure 2: Drag increase measured by a shift in the profile of mean streamwise velocity in or above the log-layer, $\Delta U^+$.

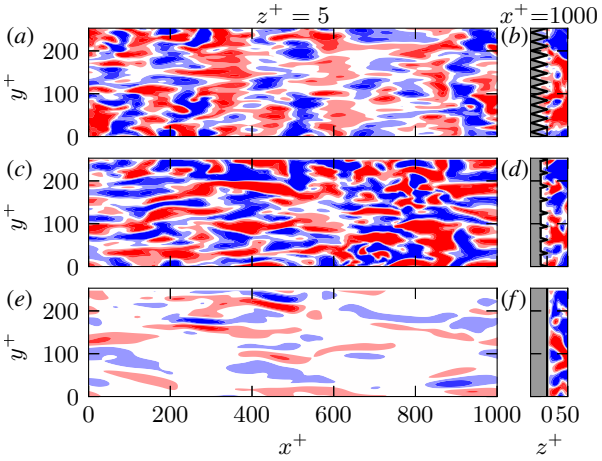


Figure 3: Visualization of Kelvin–Helmholtz rollers in wall normal velocities with contours from blue to red at $(-0.5, -0.3, -0.1, 0.1, 0.3, 0.5)w^+$ for cases TI21 ($a$, $b$), TA31 ($c$, $d$) and a smooth wall ($e$, $f$).

meters are provided in table 1 and examples of meshes are shown in figure 1. Cascade's Adapt was used to refine unstructured meshes close to the wall, where large gradients are expected. Based on a comparison of smooth-wall minimal channel results to spectra of velocity fluctuations by Moser et al. [11], we chose a streamwise grid spacing of $\Delta x^+ \approx 6$ and at least 128 tanh-spaced nodes in the wall-normal direction ($Re_\tau = 395$) to achieve similar accuracy.

In figure 2, drag increase is shown as a function of riblet size $\ell_g^+$. Reference data for triangular riblets with an opening angle $\alpha = 60°$ [1] and blade riblets with a spacing-to-thickness ratio $s/t = 4$ [5] are finely spaced along $\ell_g^+$ and illustrate the breakdown of drag-reduction with increasing riblet size. Drag changes of two cases from this study in the range $9.7 < \ell_g^+ < 23$ (▼) closely match experiments for the same geometry (▽). Expressing the riblet size by $\ell_g^+$ combines height and spacing to collapse drag curves, particularly for sizes near the drag minimum ($\ell_{g,opt}^+ \approx 10.7$) [4]. The shaded region envelops the range of slopes for small triangular riblets with $30° \le \alpha \le 90°$ according to viscous theory [9]. The drag curves of all considered riblet shapes collapse well in the drag-reducing regime and are close even in the drag-increasing regime. In order to investigate flow mechanisms that lead to a loss of performance, chosen riblet sizes start near the optimum and increase into the drag-enhancing regime.

Spanwise elongated structures resulting from a Kelvin–Helmholtz instability have been observed immediately above ($\lesssim 20\nu/u_\tau$) riblets [4] and porous surfaces [7], because the profile of mean streamwise velocity of these flows has an inflection point at the height of the roughness crest [3]. The spanwise extent of these Kelvin–Helmholtz structures can be up to about $1500\nu/u_\tau$ and their average streamwise spacing

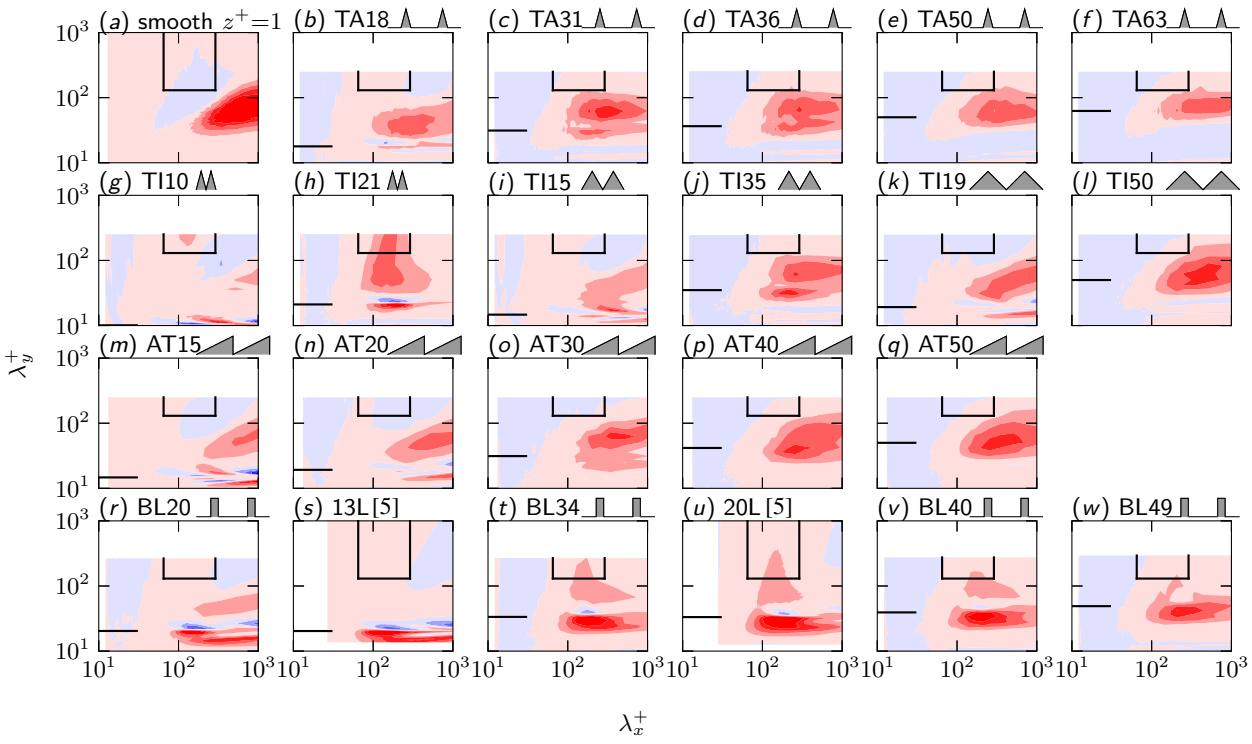


Figure 4: Premultiplied 2D co-spectra of Reynolds shear stress $-k_x^+ k_y^+ E_{uw}^+$ in the plane at the riblet crest. Normalization: $\overline{uw}^+ = \int_0^\infty \int_0^\infty E_{uw}^+ d\lambda_x^+ d\lambda_y^+$. Contours are from blue to red at $(-0.2, -0.15, -0.1, -0.05, 0, 0.05, 0.1, 0.15, 0.2)(-\overline{uw}^+)$. The horizontal lines on the left mark the riblet spacing $s$ and the open boxes near the top delimit the region of Kelvin–Helmholtz rollers ($65 < \lambda_x^+ < 290$, $\lambda_y^+ > 130$) [4]. Cases 13L (*s*) and 20L (*u*) are for channel flow data from [5].

is roughly $150\nu/u_\tau$ to $200\nu/u_\tau$ [5]. The presence of such spanwise elongated structures is visible in contours of the wall-normal velocity component at a height of $5\nu/u_\tau$ above the riblet crest. A representative flow field of the drag increasing case with sharp triangular riblets ($\alpha = 30°$) in figure 3(*a*) illustrates this spanwise coherence. For the case with equally sharp trapezoidal riblets, matched $\ell_g^+ \approx 20$ and thus comparable $\Delta U^+$ shown in figure 3(*b*), such structures are less pronounced and they are noticeably absent in flow over a smooth wall (figure 3*c*).

The Kelvin–Helmholtz instability affects a distinct spectral region of velocity and pressure fluctuations of flow over riblets with $\ell_g^+ > \ell_{g,\mathrm{opt}}^+$ [4]. Energy accumulates in streamwise wavelengths $65 < \lambda_x^+ < 290$ and spanwise wavelengths $\lambda_y^+ > 130$. Two dimensional spectra of Reynolds shear stress are shown in figure 4 for the plane at the riblet crest. The spectral region associated with the Kelvin–Helmholtz instability is framed to ease comparison between cases. For blade riblets (figure 4*r*-*w*), an increase in energy in the boxed region compared to the smooth wall is evident for all drag increasing geometries (figure 4*t*-*w*), as Kelvin–Helmholtz rollers form $\lesssim 20\nu/u_\tau$ above this plane. Almost all combinations of wavelengths in the considered spectral region transport streamwise momentum down into the groove towards the no-slip boundary. Two cases with $\ell_g^+ = 12.9$ and $\ell_g^+ = 21.3$ and a spacing-to-thickness ratio $s/t = 5$ (figure 4*r*,*t*) are compared to similar geometries at $Re_\tau \approx 550$ from [5]. The reference cases (figure 4*s*,*u*) have sizes $\ell_g^+ = 12.4$ and $\ell_g^+ = 20.4$ with $s/t = 4$. Results agree despite the much smaller domain size and lower Reynolds number of the present simulations. For triangular riblets with an opening angle $\alpha = 30°$ (figure 4*g*,*h*), energy at wavelengths associated with the Kelvin–Helmholtz instability contributes significantly to Reynolds shear stress $-\overline{uw}^+$. A peak is noticeable even for the drag-reducing size (figure 4*g*). This contribution diminishes with increasing $\alpha$ as the riblet tip becomes more blunt (figure 4*g*-*l*). For trapezoidal riblets (figure 4*b*-*f*), the portion of Reynolds shear stress in the framed spectral range is small compared to the total at this wall-normal location. With increasing riblet size, more of the short streamwise wavelengths in the considered region carry a negative contribution to $-\overline{uw}^+$ and thus transport streamwise momentum out of the groove. Asymmetric triangular riblets (figure 4*m*-*q*) also have low energy in the considered spectral region and for the larger riblets, short streamwise wavelengths convect momentum out of the groove.

In order to quantify the contribution of the spectral region associated with the Kelvin–Helmholtz instability to Reynolds shear stress, energy is integrated over previously identified wavelengths [4],

$$-\overline{uw}_{KH}^+ = -\int_{130}^{\infty}\int_{65}^{290} E_{uw}^+ d\lambda_x^+ d\lambda_y^+ . \qquad (1)$$

A balance of streamwise momentum in a control volume that fills the grooves (hatched area in sketches of table 1) shows the composition of wall shear stress, which can be written as the sum $P^+ + V^+ - \overline{uw}^+ = 1$. Here, $P^+$ is the contribution of the driving pressure gradient inside the grooves. The transport of streamwise momentum into the groove through viscous diffusion $V^+$ and the Reynolds shear stress term $-\overline{uw}^+$ are evaluated in the plane of the riblet crest, i.e. at the top of the control volume. The integral in equation (1), $-\overline{uw}_{KH}^+$ represents a portion of $-\overline{uw}^+$ and is shown in figure 5 for all riblet geometries. For the large triangular riblets with opening angle $\alpha = 30°$ (▶), approximately 6 % of wall-shear stress is a direct consequence of structures in the spectral region associated with the Kelvin–

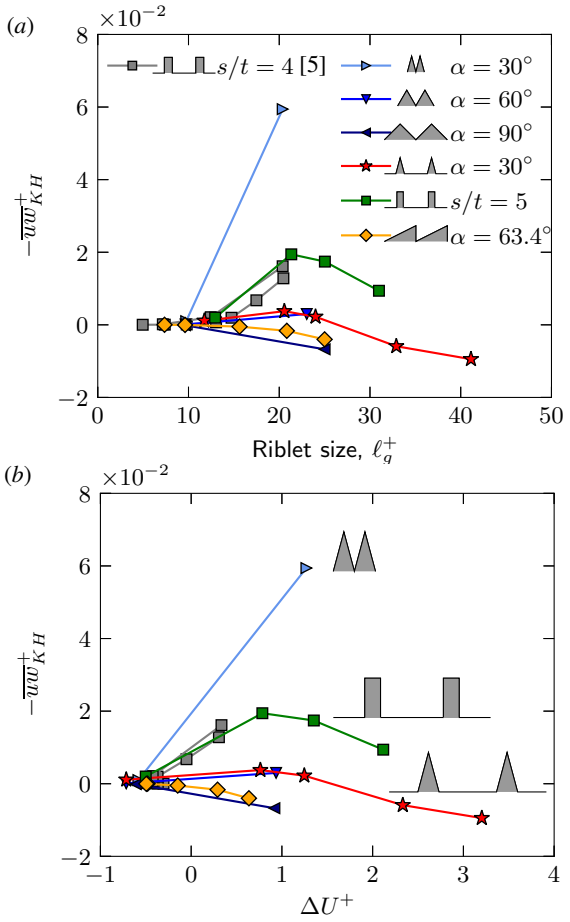


Figure 5: Contribution of Kelvin–Helmholtz rollers to the total wall-shear stress for different riblet geometries and sizes $\ell_g^+$. Reference data by [5] at $Re_\tau \approx 180$ and $Re_\tau \approx 550$.

Helmholtz instability. For blade riblets with $\ell_g^+ \approx 22$, a maximum of about 2 % is reached, but for larger geometries $-\overline{uw}^+_{KH}$ is found to decline again towards values obtained with small, drag decreasing riblets. Reference data from [5] (■) for blade riblets with $s/t = 4$ at $Re_\tau \approx 180$ and $Re_\tau \approx 550$ in figure 5 agree with present results as also seen in figure 4. In flow over trapezoidal (★) or blunt triangular riblets (▼ ◀ ◆), $-\overline{uw}^+_{KH}$ does not contribute substantially to wall-shear stress. Profiles of mean streamwise velocity for these cases have an inflection point at the height of the riblet crest and the flow field at some instances shows spanwise coherence. Nevertheless, time averaged co-spectra of Reynolds shear stress demonstrate that structures occupying the spectral region associated with the Kelvin–Helmholtz instability in the plane at the crest do not contribute to drag increase. It is apparent that the contribution of Kelvin–Helmholtz rollers to total wall-shear stress at the crest of a grooved surface depends on multiple parameters defining the riblet shape. Note that further analysis is needed to quantify the contribution of the instability to $\Delta U^+$ from all wall-normal locations. For riblet geometries with a given $\Delta U^+$ (figure 5*b*), structures resulting from the instability have high $-\overline{uw}^+_{KH}$ for sharp triangular riblets while trapezoidal riblets with the same opening angle have noticeably lower $-\overline{uw}^+_{KH}$. For geometries with small $-\overline{uw}^+_{KH}$, the breakdown of drag reduction collapses when scaled by $\ell_g^+$ (figure 2), while the large triangular riblets with high $-\overline{uw}^+_{KH}$ have a slightly different drag curve. The presence of Kelvin–Helmholtz rollers appears to promote the increase of drag with $\ell_g^+$ [4]. Riblet shapes that suppress the development of the instability seem to have a more gentle breakdown of drag reduction with increasing riblet size, which does not however affect the lowest attainable drag.

## Conclusions

Flow over riblets is generally susceptible to a Kelvin–Helmholtz instability, but the appearance of spanwise aligned rollers depends on the riblet shape. Sharp triangular and blade riblets are found to promote development of the instability, while blunt triangular or trapezoidal riblets seem to suppress it. For triangular riblets with an opening angle $\alpha = 30°$, as much as 6 % of wall-shear stress is directly attributed to Kelvin–Helmholtz structures in the plane at the riblet crest. This percentage is possibly higher for larger or sharper triangular riblets than the ones presently considered.

## Acknowledgements

This research was partially supported under the Australian Research Council Discovery Project (DP170102595) and undertaken with the assistance of resources from the National Computational Infrastructure (NCI) supported by the Australian Government and the Pawsey Supercomputing Centre with funding from the Australian Government and the Government of Western Australia. Davide Modesti was partially funded by Ermenegildo Zegna, through the "EZ Founder's Scholarship".

## References

[1] Bechert, D., Bruse, M., Hage, W., van der Hoeven, J. and Hoppe, G., Experiments on drag-reducing surfaces and their optimization with an adjustable geometry, *J. Fluid Mech.*, **338**, 1997, 59–87.

[2] Choi, H., Moin, P. and Kim, J., Direct numerical simulation of turbulent flow over riblets, *J. Fluid Mech.*, **255**, 1993, 503–539.

[3] García-Mayoral, R. and Jiménez, J., Drag reduction by riblets, *Phil. Trans. R. Soc. A*, **369**, 2011, 1412–1427.

[4] García-Mayoral, R. and Jiménez, J., Hydrodynamic stability and breakdown of the viscous regime over riblets, *J. Fluid Mech.*, **678**, 2011, 317–347.

[5] García-Mayoral, R. and Jiménez, J., Scaling of turbulent structures in riblet channels up to $Re_\tau \approx 550$, *Phys. Fluids*, **24**, 2012, 105101.

[6] Goldstein, D. and Tuan, T. C., Secondary flow induced by riblets, *J. Fluid Mech.*, **363**, 1998, 115–151.

[7] Jiménez, J., Uhlmann, M., Pinelli, A. and Kawahara, G., Turbulent shear flow over active and passive porous surfaces, *J. Fluid Mech.*, **442**, 2001, 89–117.

[8] Luchini, P., Reducing the turbulent skin friction, *Computational Methods in Applied Sciences*, **3**, 1996, 466–470.

[9] Luchini, P., Manzo, F. and Pozzi, A., Resistance of a grooved surface to parallel flow and cross-flow, *J. Fluid Mech.*, **228**, 1991, 87–109.

[10] MacDonald, M., Chung, D., Hutchins, N., Chan, L., Ooi, A. and García-Mayoral, R., The minimal-span channel for rough-wall turbulent flows, *J. Fluid Mech.*, **816**, 2017, 5–42.

[11] Moser, R., Kim, J. and Mansour, N., Direct numerical simulation of turbulent channel flow up to $Re_\tau = 590$, *Phys. Fluids*, **11**, 1999, 943–945.